Climate preconditions the Critical Zone:
Elucidating the role of subsurface fractures in the evolution of asymmetric topography

Nicole West[1], Eric Kirby[2], Andy Nyblade[3], Susan Brantley[3,4]

[1]Department of Earth and Atmospheric Sciences, Central Michigan University, [2]College of Earth Ocean and Atmospheric Sciences, Oregon State University, [3]Department of Geosciences, Pennsylvania State University, [4]Earth and Environmental Systems Institute, Pennsylvania State University

Abstract

In recent years, intensive investigation of the deep critical zone has highlighted the role that the formation and propagation of rock fractures plays in governing the evolution of critical zone architecture. Competing hypotheses invoke an interplay between tectonic and topographic stresses that enhance the potential for fractures or call on climatic variations to drive feedbacks among rock fracture, subsurface hydrology, and weathering reactions. To elucidate the processes responsible for the development of asymmetric hillslope topography and critical zone structure, we combine borehole observations of subsurface fractures and geochemical profiles with subsurface P-wave velocities modeled from seismic refraction surveys at the Shale Hills Critical Zone Observatory in central Pennsylvania. Our results reveal that P-wave velocity profiles are consistent with subsurface fracture densities and chemical depletion fronts observed in boreholes. Simple models of frost cracking show that asymmetric fracture distributions could have been achieved during past periglacial climates. Moreover, coincidence of differences in fracture density, hillslope gradient, regolith depth and regolith transport efficiency with

topographic aspect implies that mechanical damage arising from microclimatic conditions governed the long-term architecture of the Critical Zone and is manifest today in asymmetric hillslope topography.

Significance Statement

Climate controls landscape evolution by governing moisture availability for dissolution reactions and transport processes, as well as temperature conditions for weathering kinetics and cracking via thermal expansion and ice jacking. These processes conspire to set the depth and structure of the critical zone. We combine geophysical observations with direct borehole observations of bedrock fractures, and compare these observations to predictions of frost-cracking depth and intensity derived from modeled Pleistocene temperatures. Results show that depth distributions of shallow subsurface fractures correspond to major transitions in p-wave velocities with depth, and can be predicted using 1D frost cracking models. Our results further suggest that aspect-related asymmetries in regolith depth and hillslope gradient are maintained by ancient and persisting differences solar radiation.

Introduction

Climate has long been recognized as a governor of landscape evolution (1,2). Temperature fluctuations modulate diffusive processes acting along and within the interface between the solid and fluid earth; both chemical weathering of rock and soil (3-5) and dilational regolith transport via frost heave and wetting-drying cycles (6,7) exhibit a dependence on temperature. Moreover, variations in surface runoff drive sediment transport and channel incision (8-11), which in turn sets the boundary condition at the base of hillslopes. Although the interplay between these diffusive and advective regimes explains first-order characteristics of the physical structure and evolution of landscapes (12), many of the details linking physical erosion and chemical weathering (13, 14) remain unanswered (e.g., 15-17).

Recently, workers have begun to recognize the importance of the development of rock fractures as pathways that guide meteoric water infiltration and facilitate chemical weathering in the subsurface (18-21). Fractures also provide void space for biological systems to take hold, furthering weathering through chemical and physical processes (22-25). Microfractures can also grow in massive bedrock via Fe-bearing mineral dissolution, as low-density HFO phases replace primary minerals *in situ* (26, 27). Temperature fluctuations and frost-cracking are well-known to drive fracture propagation (7, 28), where water in the shallow subsurface breaks down bedrock by expansion during segregation ice growth. Finally, workers have begun to explore feedbacks between shallow stress perturbations set up by topography, tectonic stress and fracture growth (29); recent studies argue that topographically induced stresses (e.g., 30) promote systematic variations in critical zone depth that co-varies with topography (31).

Geophysical techniques have long been exploited to visualize moisture patterns and fluid pathways in the shallow subsurface (32), but recent years have seen a resurgence in the application of seismic wave propagation in the shallow subsurface to characterize the transitional boundaries between fresh and weathered bedrock (33). Because seismic velocities are dependent on the elastic properties (bulk and shear moduli) of Earth materials, in the shallowest parts of the crust, they provide constraints on in-situ mineralogy, bulk density, and porosity. Variations in P-wave velocity have been shown to correspond with fracture density and distribution in the critical zone (e.g., 33-35), and these data comprise the observational foundation for inferences relating rock fracture to hillslope stability (e.g., 36) and topographically induced stress fields (e.g., 31).

In this contribution, we combine subsurface observations from borehole and shallow seismic surveys to evaluate the hypothesis that microclimate variations govern deep critical zone structure and evolution in the Shale Hills Critical Zone Observatory (SSHO). Here, we define the critical zone as the regions of Earth's surface reaching from the tree canopy to depth of unweathered bedrock. Our previous research at the SSHO site demonstrated that systematic differences in the efficiency of dilational regolith creep on poleward- and equatorial-facing hillslopes can explain asymmetries in hillslope gradient, regolith thickness, and meteoric ^{10}Be inventories (37). However, the question of whether such differences in efficiency could be sustained over geologic timescales remains unanswered. Here, we characterize the subsurface distribution of fracturing in the shale bedrock underlying the observatory and evaluate whether fracture distributions vary with hillslope aspect. We show how relatively subtle differences in thermal forcing driven by insolation on poleward- and equatorial- facing hillslopes could drive differences in the depth of frost cracking by segregation ice. Moreover, we show that these differences are not likely to be significant under present climates, and we infer that differences in fracture depth must be the legacy of periglacial conditions during previous glacial climates. Our results thus reveal a sensitive interplay between global climate, topography and microclimate that govern fracture propagation and facilitate the advance of weathering fronts. We suggest that preconditioning of the Critical Zone by ancient climate regimes may be a significant factor in mid-latitude and alpine regions globally.

Critical Zone Architecture at the Shale Hills CZO

The Shale Hills Critical Zone Observatory (SSHO) is located in the Valley and Ridge physiographic province of the Appalachian Mountains and currently experiences a temperate climate (MAP ~1 m/yr, MAT ~ 10°C, 38). SSHO is comprised of three, small *en echelon* catchments (~ 8 ha each), developed entirely on the Rose Hill Shale, an Fe-rich, organic-poor shale deposited within the Appalachian Basin during Silurian Period (39). The SSHO watersheds are headwater catchments, bounded by ridges to the north and south, each containing westward-flowing ephemeral streams (Figure 1). Hillslopes within the SSHO exhibit a pronounced topographic asymmetry, with north-facing slopes that are systematically 5-10 degrees steeper than their south-facing counterparts (37, 41); relief on these hillslopes is typically ~30 m. Field observations reveal that augerable regolith is thicker on north-facing hillslopes than south-facing hillslopes (37, 41, 42) and is underlain by a discontinuous layer of open-framework talus. Despite this asymmetry in hillslope gradient and regolith thickness, sediment fluxes determined from accumulation of meteoric ^{10}Be within regolith (41) are similar on both north- and south-facing hillslopes (37); these relationships require that the efficiency of downslope transport is a factor of 2 greater along south-facing hillslopes. In modern climates, hillslopes in the SSHO experience more frequent freeze-thaw cycles on south-facing slopes, and these events appear to explain both differences in transport efficiency (37) and the isotopic composition of soil porewaters (43).

In the subsurface, mineralogical observations taken from a deep borehole on the north ridge of the SSHO catchment (DC-1, Figure 1) reveal a series of nested weathering fronts extending from ~ 6m below ground surface, where feldspar first appears, to ~ 20m below ground surface, where pyrite and carbonate minerals appear (20, 44, 45). Optical televiewer logs from four wells located near the valley outlet reveal considerable fracturing in the upper 6 m, but below this depth, fracture density decreases toward the bottom of the holes at ~16 m (20, 30, 46). Together, the observations of asymmetric topography and regolith transport efficiency, coupled with the apparent association between weathering fronts and fracture density, begs the questions of what process drives fracture propagation beneath the SSHO watersheds, and how fracture distribution and regolith thickness vary with landscape position.

One potentially important consideration is that the central Appalachians have experienced a long history of freeze-thaw cycling, driven by periglacial climates associated with repeated glacial advances over the past ~2 Ma. During the Last Glacial Maximum (LGM, c. 21 ky), for example, the Laurentide ice margin was located ~75 km north of SSHO. Hillslope soils developed during this time are inferred to record vigorous stirring and production of coarse detritus via frost shattering (47, 48). Similarly, widespread fields of coarse, angular talus (up to 1m in diameter) that drape hillslopes beneath quartzite ridges throughout the region appear to have developed over multiple glacial cycles (49). Colluvial wedges of coarse, subangular debris are commonly found along toe slopes; some of these deposits are classified as *greze litees* - layered, unconsolidated deposits of oriented shale fragments inferred to have formed during solifluction (47). Finally, although global scale models of Pleistocene climate suggest conditions conducive to intense frost cracking of bedrock in central Pennsylvania (50), the influence of these fluctuations in setting critical zone architecture has not been intensively investigated in this area.

Methods

To measure the depth and distribution of subsurface fractures at SSHO, we employed a combination of shallow seismic surveys along north and south facing hillslopes at SSHO with direct observations of fracture distributions in boreholes. Shallow seismic refraction surveys were conducted on four hillslopes (2 north- and 2 south-facing) and along two ridgetops within and immediately adjacent to the Shale Hills CZO catchment during field campaigns completed in 2013 and 2015. Hillslope surveys were collected along linear transects, extending from the upper hillslope (near the ridgecrest) to the toe slope; transects are co-located along geochemical (45), U-series (42, 51), and meteoric ^{10}Be (37, 41) sampling transects (Figure 1). P-wave seismic data were collected using two Geometrics Geode data loggers/seismographs with a laptop controller (Seismodule Controller). In the 2013 campaign, 36 4.5 Hz sensors were used and 48 high-frequency sensors (40 Hz geophones) were used in 2015. We used a 10 lb sledgehammer and steel plate as the seismic source in both campaigns. On hillslopes within the SSHO (both north- and south-facing hillslopes), survey lengths were 96 m, running perpendicular to topographic contours, with 2 m geophone spacing. Ridgetop surveys followed the ridge axes, and extended to 115 m long, with a 5 m geophone spacing, Surveys were also collected just outside of the central SSHO watershed (over the ridge axes) to compare velocity structures among multiple hillslopes of north- and south-facing aspect. These surveys were 67 m long with 3 m geophone spacing. Each shot location comprised 5-stacked shots to minimize noise to signal ratio.

Seismic velocity inversions were conducted using the Geometrics SeisImager/2D software (Geometrics Inc., and OYO Inc.) and were calibrated against field observations and soil pit measurements. First arrival travel times for all seismic traces were manually picked (Supplemental Materials Figure 1). From these first-arrivals, multi-layer initial models were constructed based on a simple time-term inversion of the time travel data, in which layer boundaries are visually identified based on pronounced changes in the travel-time slope, and layer velocities are based on least-square linear regressions to observed time travel data (Geometrics Inc.). (Supplemental Materials Figure 2). Time term inversions for all seismic lines produced multi-layer models with upper layer velocities of <1 km/s and lower layer velocities of

> 2km/s (Supplemental Materials Figure 3). These initial models were then used for tomographic calculations. Models were verified against p-wave velocity profiles measured along exposed walls of soil pits completed near the toe slopes of the north and south facing slopes in the SSHO watershed, where layer thicknesses could be measured (Supplemental Materials Figure 5).

To directly measure fracture density, we mapped subsurface fractures in 8 boreholes using an optical televiewer. OTV logs were completed for four deep boreholes (~16 m) located in the SSHO valley floor (CZMW 1-4, previously described in Slim et al., 2014), three shallow boreholes located along the SSHO ridgelines (CZMW 5-7, ~6 m deep), and one deep borehole located on the southern ridgeline of SSHO (~24 m deep). Fractures were identified from OTV images in WellCad (Advanced Logic Technology), a software program that also measures fracture dip angle and azimuth. Detailed descriptions of fracture dips and orientations can be found in Sullivan et al. (2017, 20). Downhole geophysical data was collected for the deep borehole completed on the southern ridge of the catchment (CZMW8, Figure 1). Geophysical logs were collected using a MGX II and Matrix acquisition system (Mount Sopris Instrument Company) and include natural gamma, fluid temperature, specific conductance, 3-arm caliper, short and long resistivity, neutron, single point resistance, spontaneous potential, optical televiewer, acoustic televiewer, density and sonic data (Supplemental Materials, Figure 4).

Imaging Critical Zone Architecture

Seismic Surveys

Seismic refraction surveys were completed along north- and south-facing hillslopes at SSHO in order to elucidate the structure of the critical zone. All seismic tomographic inversions reveal a thin, low velocity (~ 0.2 – 0.6 km/s) layer in the upper decimeters of the SSHO subsurface (Figure 2). This layer is immediately underlain by a zone characterized by steep velocity gradients, ranging from 0.6 km/s to ~ 2 km/s over depths of 2-4 m. Beneath this "gradient" zone lies a distinct transition at ~ 6-8 m depth that separates a region of uniform and fast velocities at depth from the region of steep velocity gradients within the near-surface (Figure 2).

Although the depth distributions of seismic velocity described above are observed along all sample transects, we find differences in the depth of low-velocity material on hillslopes with varying aspect. Refraction surveys consistently show that the velocity gradient along south-facing hillslopes is distributed over a relatively narrow depth range from ~ 0.5 m – 4 m depth, and the lowest-velocity layer is only observed in the uppermost 0.3 – 0.8 m. In contrast, along north-facing hillslopes, the region of low velocities near the surface is considerably thicker, approaching ~2 m, and the region of steep velocity gradients spans a greater depth range, from ~2 to 10 meters. This region appears to slightly thicken upslope toward the ridgecrest within the Shale Hills Catchment. These patterns emerge regardless of the initial condition assumed for the tomographic inversion (Figure S4), and thus they appear to represent robust characterizations of subsurface velocity structure.

In situ velocity measurements collected at hand-excavated soil pits within the SSHO reveal that P-wave velocities through soils range from 0.27 – 0.43 km/s and range from 2.12 – 3.57 km/s through intact shale bedrock (Figure S5). P-wave velocities measured through SSHO bedrock correspond well with reported P-wave velocities for intact shale from laboratory experiments (2.1 km/s - 2.7 km/s, 52), suggesting that the observed regions with P-wave velocities > 2 km/s at SSHO represent competent, intact bedrock. Similarly, P-wave velocities reported for soils and unconsolidated sediments range from 0.4 – 1.0 km/s (34), suggesting that zones of observed P-wave velocities <1 km/s at SSHO indeed represent regolith at or near the surface. Comparison of these velocity zones with auger thicknesses reported in West et al. (37, 41) and soil pit observations suggests that P-wave velocities less than 0.7 km/s correspond to the layer of regolith that is mobile under the current climate and vegetation regimes. Overall, P-wave velocity profiles at SSHO reveal uniformly thin regolith along south facing slopes, and thicker, more variable regolith depths along north-facing slopes, consistent with hand auger observations reported by West et al. (37, 41).

Direct Observations in Boreholes

Optical televiewer (OTV) logs of boreholes completed in the valley floor and along ridgetops at SSHO reveal that subsurface fractures are concentrated in the upper ~10 meters of bedrock (Figure 3, Figure S6). Peak fracture densities occur between 3 m and 8 m depth for all wells located at both valley floor and ridgetop positions (Figure 3). It should be noted that the axis of the valley in the SHHO is buried with 2 – 3 m of alluvial and colluvial material (41), whereas bedrock on ridgetops is covered by only several decimeters of regolith. Therefore, the depth of peak fracture density appears to be relatively uniform, despite regolith and/or alluvial cover. Absolute fracture counts are, however, higher in the valley floor boreholes than in the ridgetop boreholes (Figure 3).

Borehole geophysical logs of a deep well completed to 30 m in the south ridge of SSHO reveal that in zones of high fracture density, P-wave velocities are reduced by up to 40% of those recorded through intact shale bedrock (Figure S7). These results suggest that the observed P-wave transition zone in our refraction surveys are likely representative of regions of high fracture density in the SSHO subsurface. The correlation between zones of high fracture density and zones of intermediate P-wave velocity provides compelling evidence that the P-wave transition zone represents a zone of fractured and possibly chemically altered bedrock. Intriguingly, the modern extent of feldspar weathering in the SSHO (45) coincides with depth of maximum fracture densities (Figure 4).

Frost shattering and the preconditioning of the SSHO Critical Zone

Our results reveal a striking correlation between the subsurface architecture of the SSHO and the topographic asymmetry in the watershed. As noted above, our seismic surveys confirm that north-facing hillslopes are consistently mantled with thicker mobile regolith than south-facing ones across the SSHO (37). However, our data also reveal that the transitional boundary between mobile regolith and unweathered bedrock exhibits similar variation with hillslope aspect (Figure 2). On north-facing slopes, this transitional unit of intermediate P-wave velocity (0.7 – 2 km/s) thickens upslope from ~ 3 m to ~8 m (Figure 2A and C), whereas it is uniformly ~ 3 m thick along south-facing hillsides (Figure 2B and D). These transition zones thin toward the valley bottom along all hillslopes, regardless of hillslope aspect.

The correlation between P-wave velocities and fracture densities observed in boreholes suggests that these transition zones reflect the zone of high fracture density, decreasing with depth. Efforts to understand the relationship between shallow rock fracture and topographic stresses (e.g., 29, 30) suggest that focusing of stress along the convex-upward valley bottoms should generate greater fracture densities in bedrock near valley bottoms relative to ridgetops. Although this mechanism may be an explanation for the greater frequency of observed fracture in valley bottom boreholes (e.g., 30), it fails to predict the systematic differences in the depth of the velocity transition along north- and south-facing hillslopes. Similarly, more recent work incorporating regional tectonic stresses into models of stress accumulation in hilly topography, suggests that in regions of compression, subsurface stress will mirror topography, and failure potential highs are deepest under ridges, and shallow under valleys (31). Our observations do not support this hypothesis, as variations in the thickness of the transition layer occur only along the north-facing hillslopes in our study area, and are not observed on any other slope nor under the ridges. Notably, the orientation of shallow fractures in both the valley bottom and the ridgetops are largely sub-parallel with the land surface, which is consistent with either erosional unloading or with cracking during segregation ice growth (53).

These results and our previous inference of dilation-driven soil creep lead us to evaluate the potential for subsurface fracture initiation and growth via segregation ice. Ice lenses grow as liquid water held in surface tension (in soil or porous rock) is drawn toward zones of freezing in the shallow subsurface by temperature induced capillary action (18, 28, 53, 54). Under permafrost conditions, segregation ice typically produces surface parallel fractures at the depth of the active layer (53). Although the depth for fracturing is strongly controlled by surface temperatures and the availability of water (7, 28, 55), most modelling efforts predict that frost cracking can be effective to depths greater than 10 meters, peaking between 3 and 10 m in periglacial and permafrost conditions (7, 28, 55).

We predict 1-dimensional frost cracking potentials at SSHO for both modern and periglacial climate conditions, using both modern measured surface soil temperature data from SSHO and modeled surface temperature data from the Paleoclimate Modelling Intercomparison Project (phase 3, https://pmip3.lsce.ipsl.fr/; 50). Frost cracking predictions rely on the observation that a "frost-cracking window" exists in bedrock at temperatures between -8 and -3

°C (56). The product of the subsurface temperature gradient and the time rock spends within the frost-cracking window can be notionally considered as a frost-cracking potential (°C/cm-days) (e.g, 18, 28, 55). 1-dimensional annual thermal gradient models were constructed for SSHO using the equation:

$$T(z,t) = MAT + Tae^{-z\sqrt{\frac{\pi}{\alpha P_y}}} \sin\left(\frac{2\pi t}{P_y} - z\sqrt{\frac{\pi}{\alpha P_y}}\right)$$

where T is temperature (°C), t is time, z is depth, MAT is mean annual temperature, Ta is the amplitude in annual temperature swings (°C), α is the thermal diffusivity of rock (900 $Ccm^{-2}d^{-1}$ for shale, 57), and P_y is period of the sinusoid (365d). This model assumes exposed rock at the surface, and thus does not account for the insulating effects of soils or snowpack.

To model Pleistocene thermal gradients, we used modeled mean annual surface temperatures (50), which for central Pennsylvania are reported between 15 and 20 °C below modern MATs of 10 °C. In order to estimate temperature differences with respect to aspect, as well as potential surface temperature swings, we relied on differences recorded in modern environments proximal to permafrost zones. On bare bedrock exposures near Fairbanks, AK, surface temperatures can vary by up to 4 °C between north and south facing hillslopes (58). Similarly, annual swings in surface temperature have been shown to be affected by aspect. On the Tibetan Plateau, surface soils can span temperature amplitudes of up to 15 °C for north-facing slopes and 17 °C for south-facing slopes (59). Using these modern periglacial analogs along with modeled mean annual temperatures for the late Pleistocene, we conservatively constrain our model values within the boundaries established in the literature, at -6.5 ± 12°C for the north-facing slope and -2.5 ± 16°C for the south-facing slope at SSHO.

Our models of frost cracking potential in the modern climate regime, using measured surface temperatures from the north and south hillslopes at SSHO, suggest that frost action peaks at depths less than 1 meter, falling to zero below ~1 m of rock (Figure 5A and B). This result suggests that freezing conditions in the present-day climate are insufficient to generate the observed fracture patterns. However, when we consider likely late Pleistocene temperature conditions, the region of enhanced frost cracking potential extends to ~ 10 m depth and exhibits a distinct maximum between 3 m and 6 m depth (Figure 5C and D). The consistency between predicted frost-cracking during periglacial temperature conditions and observed fracture density patterns in both ridgetop and valley floor boreholes suggest the present-day architecture of the SSHO critical zone reflects the imposition of a prior climate history.

Frost cracking also appears to explain differences in the depth of fracturing on hillslopes with opposite aspect. By combining the observed differences in seasonal temperature swings between the north and south facing hillslope at SSHO, and the modeled MAT values for the region during the late Pleistocene, we predict slight differences the depth of fracture penetration with respect to hillslope aspect. Our models suggest that reduced insolation on north-facing slopes leads to lower average temperatures throughout the temperature profile (Figure 5C) that maintain temperatures well within the frost cracking window to somewhat greater depth. We suggest that open-framework layers of shattered rock observed at the regolith/bedrock boundary on north-facing slopes in and around the SSHO (37, 41) are a manifestation of deeper penetration of frost shattering on these slopes. Our results are consistent with previous work suggesting that frost cracking may reach to depths of 10 m at mean annual temperatures of -5°C (28); these conditions were likely representative of periglacial conditions at the SSHO during Pleistocene glacial maxima (50).

Our geophysical characterization of the SSHO subsurface provides a physical mechanism that explains linkages between surficial geochemical and geophysical observations and geochemical observations at depth. We argue that frost shattering during periglacial conditions at the SSHO "pre-conditioned" rocks in the near subsurface by generating a network of fractures, that were subsequently exploited by shallow subsurface flow during the transition to warmer conditions during the late Pleistocene and Holocene. Along south-facing slopes, more frequent thawing events provided an efficient mechanism to transport coarse debris produced by frost shattering down hillslopes to the channel, where they could be conveyed out of the watershed. Conversely, on north-facing slopes, frost-shattered debris remained frozen, relatively immobile, and available for continued frost action. On both north- and south-facing hillslopes, fractures generated by ice provided pathways for penetration of meteoric fluids to depth, and may have dictated the initial depth of chemical reaction fronts. Given sufficient time, and subject to similar asymmetries in regolith transport efficiency during interglacial periods (37), these processes appear to have conspired to drive hillslopes toward their current topographic asymmetry. Our results thus reinforce the notion that asymmetry in Critical Zone architecture co-evolves with landscape topography as a consequence of microclimatic conditions (7).

Our results also provide a plausible explanation for global observations of topographic asymmetry in mid-latitudes. Intravalley asymmetry is ubiquitous along the Western Cordillera between ~15 and 50 degrees latitude (e.g., 60), characterized by polar-facing hillslopes that stand steeper than their equatorial-facing counterparts. Our results suggest that these first-order features of global topography likely owe their origin to the interplay among microclimate, rock shattering, and erosional efficiency sustained throughout the glacial/interglacial cycles of the Pleistocene.

Conclusions

Geophysical surveys provide key insights into how processes occurring in Earth's shallow subsurface are fundamental to the structural evolution of the critical zone. Our results suggest that fracturing in the SSHO subsurface played an integral part in the physical and chemical evolution of the watershed. P-wave velocities reveal systematic differences in patterns of regolith and fracture thickness with respect to aspect at SSHO. The depth and spatial distribution of inferred fracture density suggest that shattering of rock during periglacial conditions of the Pleistocene likely primed the hillslopes at SSHO for physical and chemical soil development during Holocene time. Fracturing during frost cracking events perhaps even was a necessary driver for the observed aspect-related topographic asymmetry and differences in chemical weathering rates on north and south facing hillslope at SSHO. It seems clear that the legacy of climate change and its impact on the landscape exerts a first-order control on the modern architecture and functioning of the Critical Zone.

Acknowledgements

This research was funded by NSF Grant EAR 13-31726 to S.L. Brantley. This research was conducted in Penn State's Stone Valley Forest, which is funded by the Penn State College of Agriculture Sciences, Department of Ecosystem Science and Management and managed by the staff of the Forestlands Management Office.

References

1. Gilbert, G.K. (1904) Systematic asymmetry of crest lines in the High Sierra of California: The Journal of Geology, v. 12, 579–588, doi:10.1086/621182.

2. Gilbert, G.K. (1909), The convexity of hilltops, Journal of Geology, 17, 344-350.
3. White, A.F., Blum, A.E., (1995), Effects of climate on chemical weathering in watersheds, Geochimica nad Cosmochimica Acta, v. 59(9), 1729-1747.
4. Riebe, C.S., J.W. Kirchner, R.C. Finkel (2004), Erosional and climatic effects on long-term chemical weathering rates in granitic landscapes spanning diverse climate regimes, Earth and Planetary Science Letters, 224(3-4), 547 – 562.
5. West, A.J., Galy, A., Bickle, M. (2005), Tectonic and climatic controls on silicate weathering, Earth and Planetary Science Letters, 235(1-2), 211 – 228.
6. Kirkby, M.J., (1967), Measurement and theory of soil creep, Journal of Geology, v.75(4), 359-378.
7. Anderson, R.S., Anderson, S.P., and Tucker, G.E., (2013), Rock damage and regolith transport by frost: An example of climate modulation of the geomorphology of the critical zone: Earth Surface Processes and Landforms, v. 38, 299–316, doi:10.1002/esp.3330.
8. Molnar,P., Brown, E.T., Burchfield, B.C., Deng, Q., Feng, X., Li, J., Raisbeck, G.M., Shi, J., Zhangming, W., Yiou, F., You, H. (1994), Quaternary Climate Change and the Formation of River Terraces across Growing Anticlines on the North Flank of the Tien Shan, China, The Journal of Geology, v. 102(5), 583-602
9. Rinaldo, A., Dietrich, W. E., Rigon, R., Vogel, G. K., RodriguezIturbe, I. (1995), Geomorphological signatures of climate, Nature, v. 374, 632-635.
10. Whipple, K. X., and G. E. Tucker (1999), Dynamics of the stream-power river incision model: Implications for height limits of mountain ranges, landscape response timescales, and research needs, J. Geophys. Res., 104(B8), 17661–17674, doi:10.1029/1999JB900120.
11. Hartshorn, K., Hovius, N., Dade, B.D., Slingerland, R.L., (2002), Climate-Driven Bedrock Incision in an Active Mountain Belt, Science, v. 297, No. 5589, 2036-2038
12. Perron, J.T., J.W. Kirchner, W.E. Dietrich (2009), Formation of evenly spaced ridges and valleys. Nature, v. 460, 502-505.
13. Stallard, R.F., J.M. Edmond (1983), Geochemistry of the Amazon 2. The influence of geology and weathering environment on the dissolved load, Journal of Geophysical, v. 88(NC14), 9671 – 9688.
14. Raymo, M.E., W.F. Ruddiman (1992), Tectonic forcing of late Cenozoic climate, Nature, v. 359 (6391), 117 – 122, doi:10.1038/359117a0.
15. Ferrier, K.L., Kirchner, J.W. (2008), Effects of physical erosion on chemical denudation rates: A numerical modeling study of soil-mantled hillslopes, Earth and Planetary Science Letters, v. 272, 591 – 599.
16. Dixon, J.L., Hartshorn, A.S., A.M. Heimsath, R.A. DiBiase, K.X. Whipple (2012), Chemical weathering response to tectonic forcing: A soils perspective from the San Gabriel Mountains, California, Earth and Planetary Science Letters, v. 323 – 324, 40 – 49.
17. Larsen, I.J., Almond, P.C., Eger, A., Stone, J.O., Montgomery, D.R., Malcolm, B., (2014), Rapid Soil Production and Weathering in the Southern Alps, New Zealand, Science, v. 343, 637-640.
18. Anderson, R.S., (2002), Modeling of tor-dotted crests, bedrock edges and parabolic profiles of the high alpine surfaces of the Wind River Range, Wyoming, Geomorphology, v. 46, 35–58.
19. Riebe, C.S., Hahm, W.J., Brantley, S.L., (2016), Controls on deep critical zone architecture: a historical view nad four testable hypotheses, Earth Surface Processes and Landforms, DOI: 10.1002/esp.4052

20. Sullivan P.L., Hynek, S., Gu, X., Singha, K., White, T., West, N., Kim, H., Clarke, B., Kirby, E., Duffy, C., Brantley, S.L., (2016), Oxidative dissolution under channel leads geomorphological evolution at the Shale Hills Catchment, American Journal of Science, v. 316, 981-1026. doi:10.2475/10.2016.02.
21. Eppes, M., Keanini, (2017), Mechanical weathering and rock erosion by climate-dependent subcritical cracking, Reviews of Geophysics, v. 55, 470-508, doi:10.1002/2017RG000557
22. Zwieniecki MA, Newton M., (1994), Root distribution of 12-year-old forests at rocky sites in southwestern Oregon: effects of rock physical properties. Canadian Journal of Forest Research, v. 24, 1791–1796.
23. Zwieniecki MA, Newton M., (1995), Roots growing in rock fissures: their morphological adaptation. Plant and Soil, v. 172, 181–187.
24. Matthes-Sears, U., Larson, D.W., (1995), Rooting Characteristics of trees in rock: a study of Thuja Occidentalis on cliff faces, International Journal of Plant Sciences, v. 156(5), 679-686.
25. Hasenmueller, E., Gu, X., Weitzman, J., Adams, T. Stinchcomb, G., Eissenstat, D., Drohan, P., Brantley, S., and Kaye, J., (2017), Weatheirng of rock to regolith: The activity of deep roots in bedrock, Geoderma, v. 300, 11-31.
26. Eggler, D.H., Larson, E.E., Bradley, W.C. (1969), Granites Grusses and Sherman Erosion Surface Southern Laramie Range Colorado-Wyoming. Am J Sci v. 267, 510–522.
27. Fletcher, R.C., Buss, H., Brantley, S.L. (2006), A spheroidal weathering model coupling porewater chemistry to soil thicknesses during steady-state denudation, Earth and Planetary Science Letters, v. 244(1-2), 444 – 457, doi: 10.1016/j.epsl.2006.01.055.
28. Hales, T. C., and J. J. Roering (2007), Climatic controls on frost cracking and implications for the evolution of bedrock landscapes, J. Geophys. Res., v. 112, F02033, doi:10.1029/2006JF000616.
29. M Miller, D. J., & Dunne, T. (1996). Topographic perturbations of regional stresses and consequent bedrock fracturing. Journal of Geophysical Research: Solid Earth, v. 101(B11), 25523-25536.
30. Slim, M., Perron, J. T., Martel, S. J., & Singha, K. (2015). Topographic stress and rock fracture: a two dimensional numerical model for arbitrary topography and preliminary comparison with borehole observations. Earth Surface Processes and Landforms, v. 40(4), 512-529.
31. St. Clair J., Moon S., Holbrook W. S., Perron J. T., Riebe C. S., Martel S. J., Carr B., Harman C., Singha K., Richter D. deB. (2015). Geophysical imaging reveals topographic stress control of bedrock weathering. Science, v. 350(6260), 534-538.
32. Hubbard and Rubin, (2002), Hydrogeophysics: state of the discipline, EOS, v.83(51), 602-606.
33. Holbrook, W.S., Riebe, C.S., Elwaseif, M., Hayes, J.L., Basler-Reeder, K., Harry, D.L., Malazian, A., Dosetto, A., Hartsough, P.C., Hopmans, J.W., (2014), Geophysical constraints on deep weathering and water storage potentital in the southern sierra critical zone observatory, Earth Surface Processes and landforms, v. 39, 366-380, DOI: 10.1002/esp.3502
34. Befus, K.M., Sheehan, A.F., Leopold, M., Anderson, S.P., Anderson, R.S., (2011), Seismic contraints on critical zone architecture, Boulder Creek watershed, Front Range, Colorado, Vadose Zone Jouranl, v. 10, 915-927, doi:10.2136/vzj2010.0108
35. Parsekian, A.D., Singha, K., Minsley, B.J., Holbrook, W.S., Slater, L., (2015), Multiscale geophysical imaging of the critical zone, Review of Geophysics, v. 53, doi:10.1002/2014RG000465.

36. Clarke, Brian A, & Burbank, Douglas W. (2011). Quantifying bedrock-fracture patterns within the shallow subsurface: Implications for rock mass strength, bedrock landslides, and erodibility. Journal of Geophysical Research., v. 116(F4)

37. West, N., Kirby, E., Bierman, P., Clarke, B., (2014), Aspect-dependent variations in regolith creep revealed by meteoric ^{10}Be, Geology, doi:10.1130/G35357.1

38. Arguez, A., Durre, I., Applequist, S., Squires, M., Vose, R., Yin, X., Bilotta, R., (2010) NOAA's U.S. Climate Normals (1981-2010). NOAA National Centers for Environmental Information. DOI:10.7289/V5PN93JP

39. Swain, F.M. (1966), Coal Science, Distribution of some organic substances in Paleozoic rocks of Central Pennsylvania, 1-21, American Chemical Society, Washington, D.C.

40. Meyer, S.C., D.A. Textoris, J.M. Dennison (1992), Lithofacies of the Silurian Keefer Sandstone, east-central Appalachian basin, USA, Sedimentary Geology, v. 76, 187 – 206.

41. West, N., Kirby, E., Bierman, P., Slingerland, R., Ma, L., Rood, D., and Brantley, S., (2013), Regolith production and transport at the Susquehanna Shale Hills Critical Zone Observatory, Part 2: Insights from meteoric ^{10}Be: Journal of Geophysical Research, doi:10.1002/jgrf.20121.

42. Ma, L., F. Chabaux, L. Jin, N. West, E. Kirby, S. Brantley (2013), Regolith production and transport at the Susquehanna Shale Hills Critical Zone Observatory – Part 1: insights from U-series isotopes, Journal of Geophysical Research – Earth Surface, v. 118, doi:10.1002/jgrf.20037.

43. Thomas, E. M., Lin, H., Duffy, C.J., Sullivan, P.L., Holmes, G.H., Brantley, S.L., Jin, L. (2013) Spatiotemporal patterns of water stable isotope compoistions at the Shale Hills Critical Zone Obseratory: Linkages to subsurface hydrologic processes, Vadose Zone Journal, doi:10.2136/vzj2013.01.0029

44. Jin, L., R. Ravella, B. Ketchum, P.R. Bierman, P. Heaney, T. White, S.L. Brantley (2010), Mineral weathering and elemental transport during hillslope evolution at the Susquehanna/Shale Hills Critical Zone Observatory, Geochimica et Cosmochimica Acta, v. 74, 3669-3691.

45. Brantley, S. L., Holleran, M. E., Jin, L. and Bazilevskaya, E. (2013), Probing deep weathering in the Shale Hills Critical Zone Observatory, Pennsylvania (USA): the hypothesis of nested chemical reaction fronts in the subsurface. Earth Surf. Process. Landforms, v. 38: 1280–1298. doi:10.1002/esp.3415

46. Kuntz, B., Rubin, S., Berkowitz, B., and Singha, K. (2011) Quantifying Solute Transport at the Shale Hills Critical Zone Observatory, Vadose Zone Journal, v. 10:843-857

47. Clark, G.M., E.J. Ciolkosz (1988), Periglacial geomorphology of the Appalachian highlands and interior highlands south of the glacial border – A review, Geomorphology, v. 1, 191 – 220.

48. Braun, D.D. (1989), Glacial and periglacial erosion of the Appalachians, Geomorphology, v. 2, 233–256.

49. Denn, A.R., Bierman, P.R., Zimmerman, S.R.H., Corbett, L.B., and Kirby, E., (in press), Cosmogenic nuclides indicate that boulder fields are dynamic, ancient, multigenerational features: GSA Today, v. 28, doi: 10.1130/GSATG340A..1.

50. Braconnot, P., S. P. Harrison, M. Kageyama, P. J. Bartlein, V. Masson-Delmotte, A. Abe-Ouchi, B. Otto-Bliesner, and Y. Zhao (2012), Evaluation of climate models using palaeoclimatic data, Nat. Clim. Change, v. 2(6), 417–424, doi:10.1038/Nclimate1456.

51. Ma, L., F. Chabaux, E. Pelt, E. Blaes, L. Jin, S. Brantley (2010), Regolith production rates calculated with uranium-series isotopes at Susquehanna/Shale Hills Critical Zone Observatory, Earth and Planetary Science Letters, v. 297, 211-225.

52. Press, F., (1966), Seismic Velocities, in Clark, S.P., Jr, Ed. Handbook of physical constants, GSA Mem., v. 97, 195-218.

53. Murton, J.B., Peterson, R., Ozouf, J.C., (2006), Bedrock fracture by segregation ice growth in cold regions, Science, v .314(5802), 1127-1129.
54. Marshall, J.A., Roering, J.J., BartleinP.J., Gavin, D.G., Granger, D.E., Rempel1, A.W., Praskievicz, S.J., Hales, T.C., (2015), Frost for the trees: Did climate increase erosion in unglaciated landscapes during the late Pleistocene?, Science Advances, DOI: 10.1126/sciadv.1500715
55. Rempel, A.W., Marshall, J.A., Roering, J.J., (2016), Modeling relative frost weathering rates at geomorphic scales, Earth and Planetary Science Letters, v. 453, p. 87-95.
56. Hallet, B., J. Walder, and C. W. Stubbs (1991), Weathering by segregation ice growth in microcracks at sustained sub-zero temperatures: Verification from an experimental study using acoustic emissions, Permafrost Periglacial Processes, 2, 283–300.
57. Clark, S.P., Jr., (1966), Ed. Handbook of physical constants, GSA Mem., v. 97
58. Collins, C.M., Haugen, R.K., Kreig, R.A., (1988), Natural ground temperatures in upland bedrock terrain, interior Alaska, Proceedings, 6th International Conference on Permafrost, Trondheim, Norway, v. 1, 56-60.
59. Xinsheng Liu, X. and Luo, T., (2011), Spatiotemporal Variability of Soil Temperature and Moisture across two ContrastingTimberline Ecotones in the Sergyemla Mountains, Southeast Tibet, Arctic, Antarctic, and Alpine Research, v. 43(2), 229-238
60. Poulos, M.J., Pierce, J.L., Flores, A.N., and Benner, S.G., (2012), Hillslope asymmetry maps reveal widespread, multi-scale organization: Geophysical Research Letters, v. 39, L06406, doi:10.1029/2012GL051283.

Figure Captions

Figure 1. Slope map of the SSHO created from high resolution LiDAR topography (pasda.psu.edu), showing topographic asymmetry, with steeper north-facing slopes than south-facing slopes. Black lines correspond to seismic survey locations across the north and south ridges at SSHO. Borehole locations indicated by white circles.

Figure 2. Modeled P-wave tomography of the north and south facing hillslopes in and adjacent to the SSHO. P-wave results show thin low velocity units on south facing slopes that are thicker on their north facing counterparts. Thick black lines mark the 2.0 km/s contour, and thin black lines mark 0.6 km/s contour.

Figure 3. Probability density plots of fracture occurrence in all 8 wells at SSHO. Warm color lines indicate ridgetop well fracture probabilities (red field shows sum of all ridgetop wells), while cool color lines show valley well probabilities (blues field shows sum of all valley wells). Thick black line shows the summed probability of all fracture occurrences with depth. Plots show peak fracture densities between 3 m and 6 m in both valley and ridgetop wells; however, fracture frequency is higher in the valley wells. CZMW8 is excluded as the well is cased to 18m, and no fracture counts could be collected to that depth.

Figure 4. Depth profiles of average modeled 1D P-wave velocities proximal to the CZMW8 borehole on the south ridge of SSHO (blue line) with tau values for Mg (green circles) and K (purple circles) for from chips collected during drilling of CZMW8. Stacked histograms of fracture counts from shallow wells shown in red.

Figure 5. A) Thermal gradients in bedrock under modern temperature conditions at SSHO. MAT and temperature amplitudes are derived from measured surface soil temperatures for the north and south facing slopes in the SSHO watershed (blue and red lines, respectively; CITE) B) Frost-cracking potentials under modern temperature conditions at SSHO for north and south facing slopes (blue and red lines, respectively). C) Thermal gradients in SSHO subsurface under assumed temperature conditions for SSHO under periglacial climate. MATs derived from PMIP model outputs for 20 ka, and temperature amplitudes are estimated from modern periglacial soil data (CITES, see supplemental?) D) Frost-cracking potentials under assumed periglacial temperature conditions.

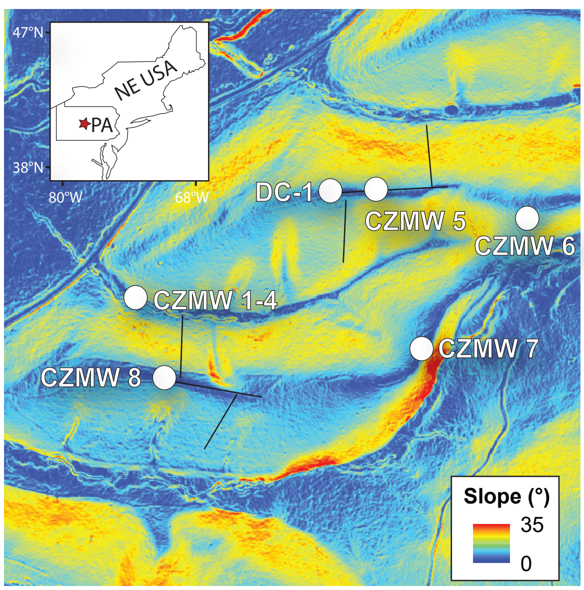
47°N
38°N
80°W
68°W
NE USA
PA
DC-1
CZMW 5
CZMW 6
CZMW 1-4
CZMW 7
CZMW 8
Slope (°)
35
0

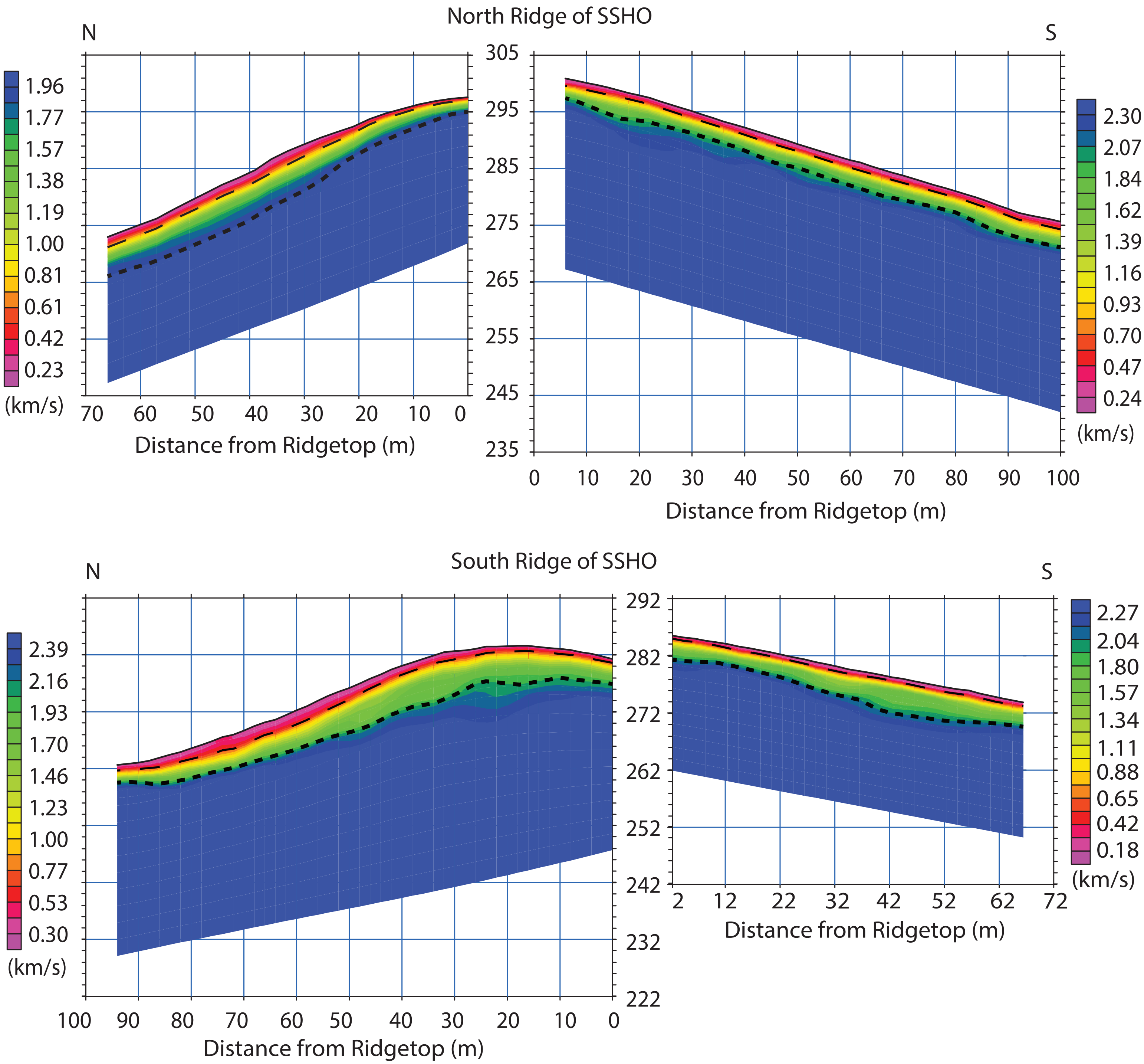
North Ridge of SSHO
N
S
1.96
1.77
1.57
1.38
1.19
1.00
0.81
0.61
0.42
0.23
(km/s)
70 60 50 40 30 20 10 0
Distance from Ridgetop (m)
305
295
285
275
265
255
245
235
0 10 20 30 40 50 60 70 80 90 100
Distance from Ridgetop (m)
2.30
2.07
1.84
1.62
1.39
1.16
0.93
0.70
0.47
0.24
(km/s)
South Ridge of SSHO
N
S
2.39
2.16
1.93
1.70
1.46
1.23
1.00
0.77
0.53
0.30
(km/s)
100 90 80 70 60 50 40 30 20 10 0
Distance from Ridgetop (m)
292
282
272
262
252
242
232
222
2 12 22 32 42 52 62 72
Distance from Ridgetop (m)
2.27
2.04
1.80
1.57
1.34
1.11
0.88
0.65
0.42
0.18
(km/s)

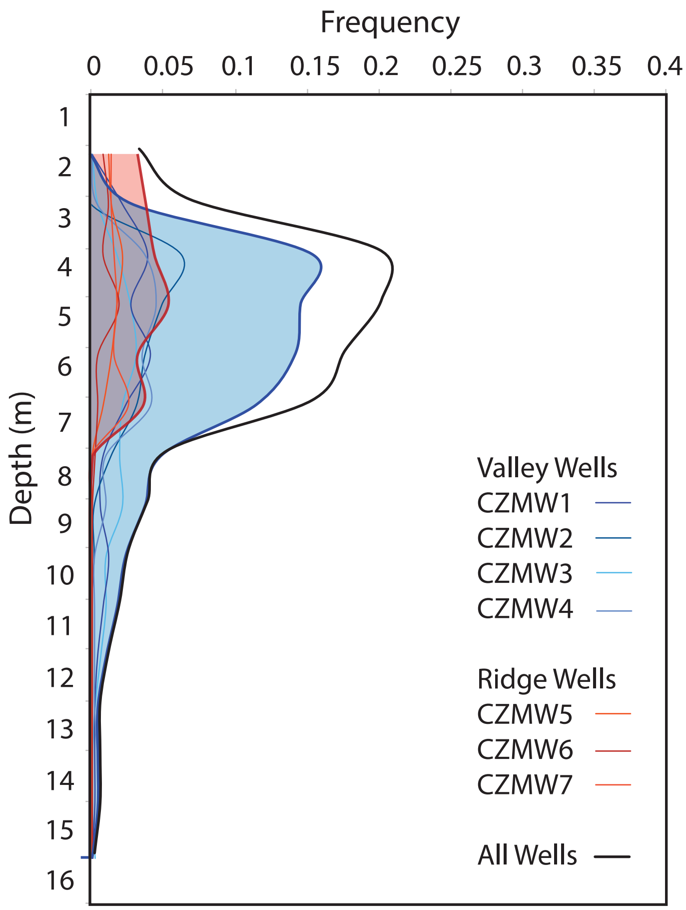

Frequency
0
0.05
0.1
0.15
0.2
0.25
0.3
0.35
0.4
Depth (m)
1
2
3
4
5
6
7
8
9
10
11
12
13
14
15
16
Valley Wells
CZMW1
CZMW2
CZMW3
CZMW4
Ridge Wells
CZMW5
CZMW6
CZMW7
All Wells

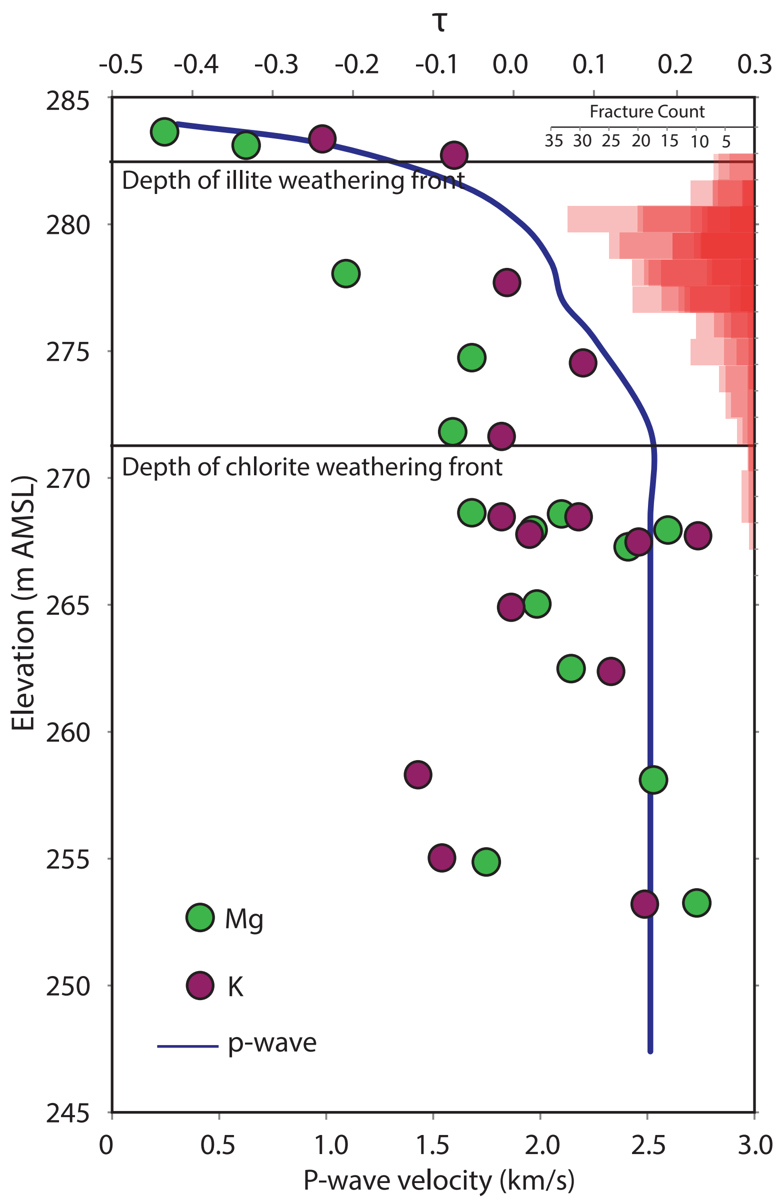

τ
-0.5 -0.4 -0.3 -0.2 -0.1 0.0 0.1 0.2 0.3
Fracture Count
35 30 25 20 15 10 5
Depth of illite weathering front
Depth of chlorite weathering front
285 280 275 270 265 260 255 250 245
Elevation (m AMSL)
Mg
K
p-wave
0 0.5 1.0 1.5 2.0 2.5 3.0
P-wave velocity (km/s)

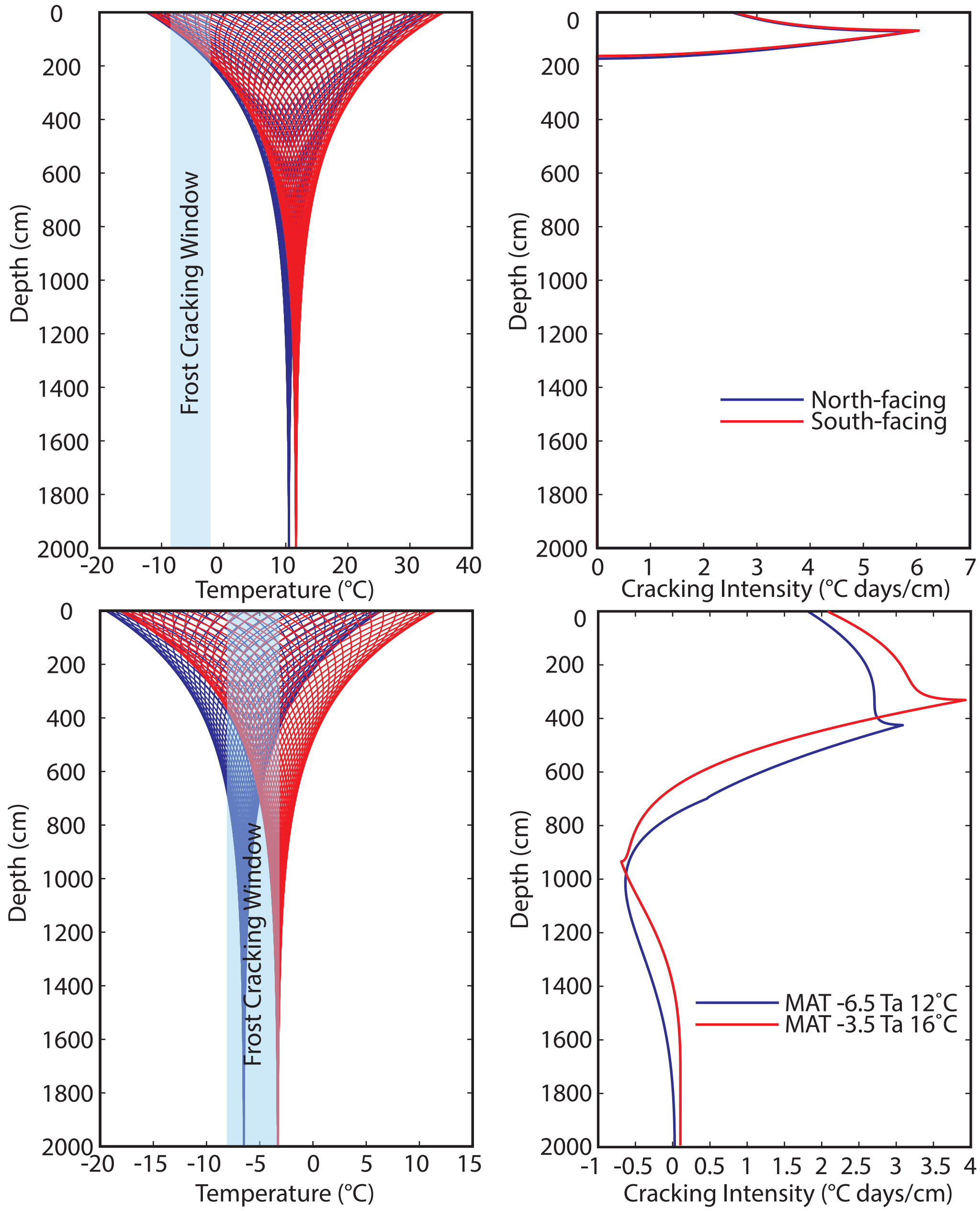
Frost Cracking Window
Depth (cm)
Temperature (°C)
Cracking Intensity (°C days/cm)
North-facing
South-facing
Frost Cracking Window
Depth (cm)
Temperature (°C)
Cracking Intensity (°C days/cm)
MAT -6.5 Ta 12°C
MAT -3.5 Ta 16°C

Supplemental Materials

Analysis of geophysical data

Shallow p-wave refraction survey data was processed using SeisImager/2D software by Geometrics, Inc. First returns were handpicked using the Pickwin module (Figure S1) and results were imported into the Plotrefa module for travel time and (Figures S2, S3). We evaluated multiple starting models, implementing both linear and layered models to address the sensitivity of the tomographic inversion results to initial conditions (Figure S4). Root mean squared errors (RMSE) for all starting models fell between 2.09 and 2.21 ms, with the lowest RMSE recorded for the layered models. The depth of the 2.0 km/s line varied slightly between models, appearing at greater depths where we imposed a linear gradient in p-wave velocity with depth. In these cases, the depth of the 2.0 km/s line fell between 6 and 8 m, deepening with increasing depth to lowest layer (DTTL). Depth to the 2.0 km/s line in the layered model crosses between 4 and 5 m. Depth to the 0.6 km/s line remained at just under 2 m for all models. These differences do not significantly affect our interpretations of fracture depths in the SSHO subsurface.

In situ velocities

Numerous shallow pits were completed at SSHO to or near the fractured bedrock surface, providing the opportunity to observe p-wave velocities through known depths of soil and rock. From these measurements, we see that at the base of the south- facing slope of SSHO, there is a 62 ± 25 cm thick layer of soil with a p-wave velocity of 0.32 ± 0.03 km/s on top bedrock with a velocity of 2.85 ± 1.02 km/s (n=2). In the pit completed on the north-facing slope of SSHO, we find a 1.39 ± 0.19 m thick colluvial layer with a p-wave velocity of 0.34 ± 0.01 km/s overlying bedrock with p-wave velocities of 2.43 ± 0.75 km/s (n=9). Transition depths were calculated assuming a two layer system with a horizontal contact. Examples of the travel time curves are shown in Figure S5.

Borehole Observations

Fracture densities were recorded with depth in 7 boreholes completed at SSHO, using optical televiewer imaging (Figure S6). Optical televeiewers utilize a 360° camera and can record the depth dip and azimuth of fractures. Total counts per unit depth were used to calculate fracture occurrence probabilities in the wells with respect to depth. CZMW8, the deep well completed on the south ridge of the SSHO catchment was cased to 18 m, and was therefore omitted from fracture analysis. However, downhole seismic data shows that in zones of high fracture density, seismic velocities decrease nearly 40% (Figure S7).

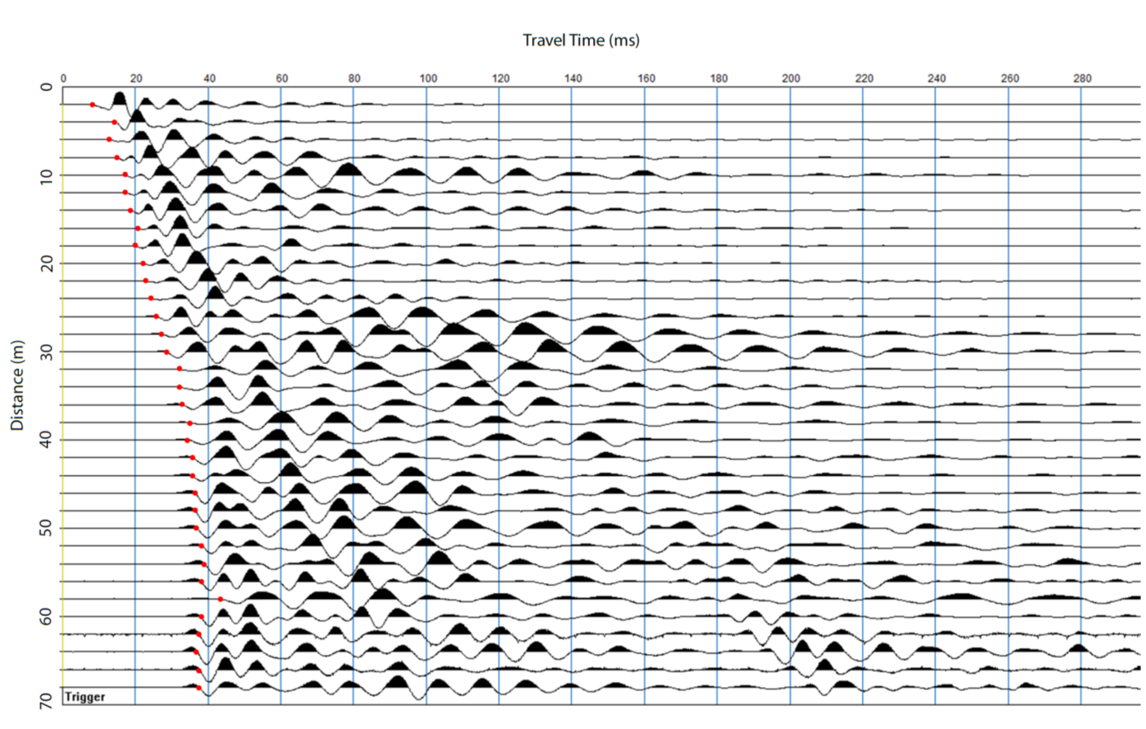

Figure S1. Example of seismic waves in the SSHO subsurface. Y axis shows distance from shot point in meters and x axis show travel time in milliseconds. Red dots indicate the hand-picked first returns used to calculate the initial P-wave model. The wave pattern shown here is characteristic of increasing P-wave velocities with depth observed throughout SSHO.

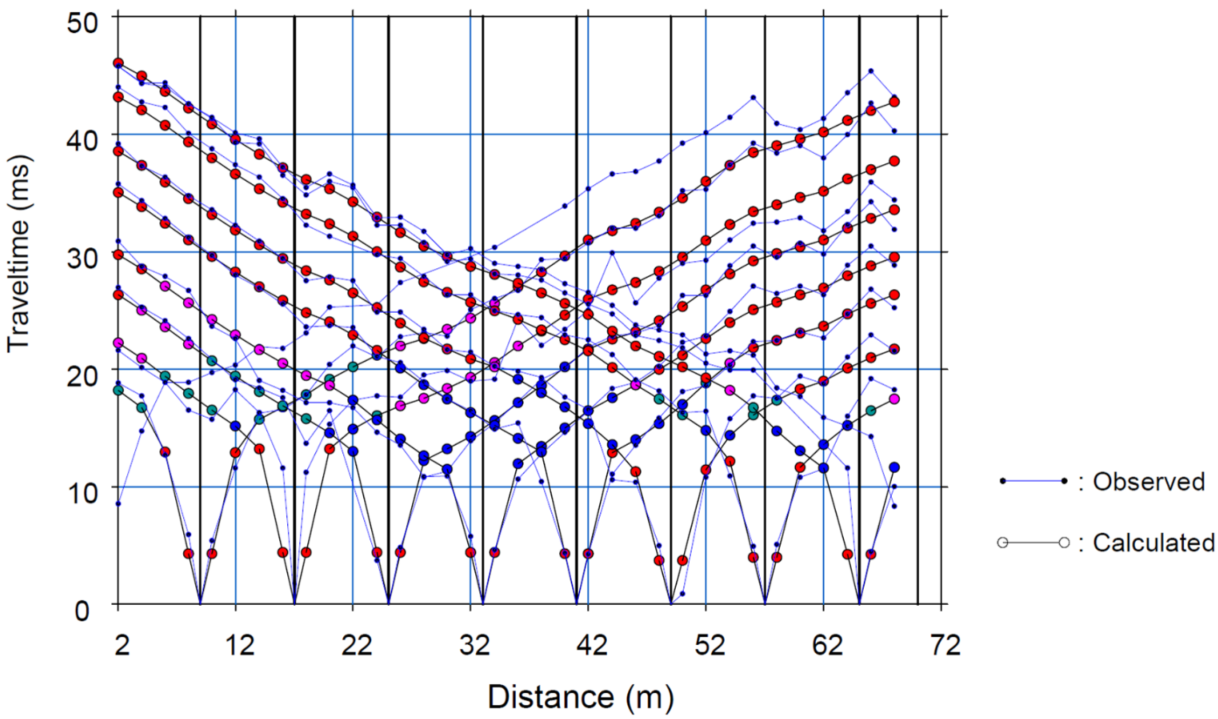

Figure S2. Example travel time curves calculated from first returns picked for the south facing hillslope within SSHO. The thin blue lines correspond to observed (picked) values and the thick black lines correspond to model calculations based on observations. The slope breaks indicate velocity transitions between subsurface layers. These breaks inform depths and velocities of layered initial models.

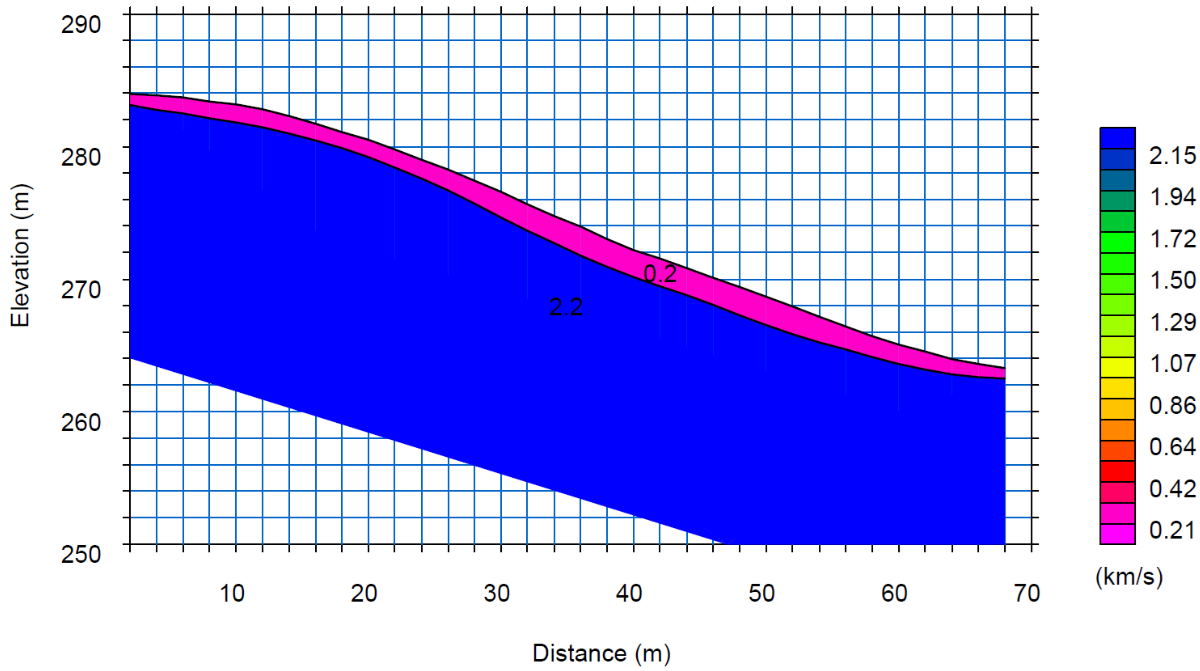

Figure S3. Example of an initial layered model for the north-facing hillslope within SSHO. The model was produced from travel time slope breaks similar to those pictured in Figure S2.

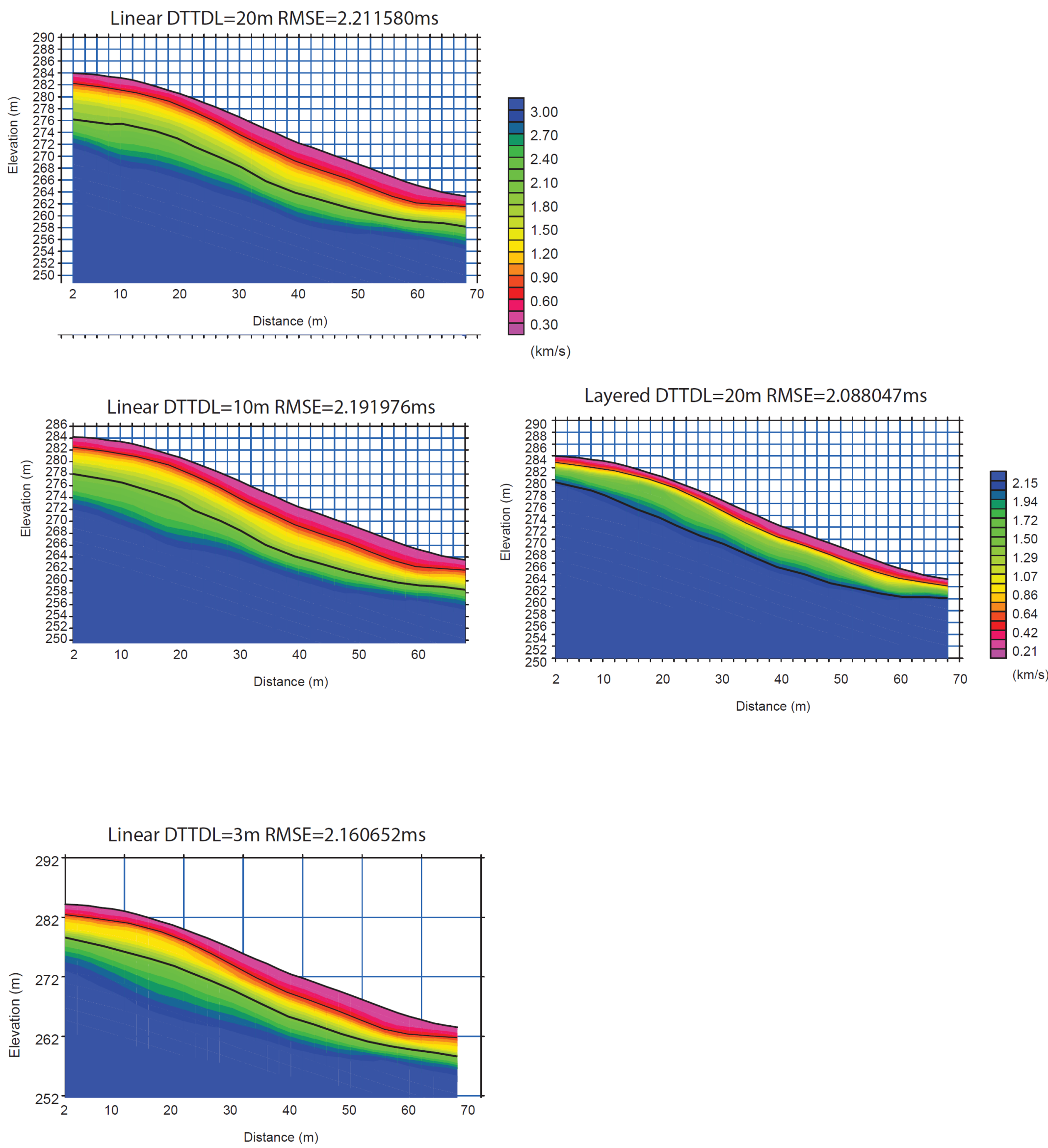

Figure S4. Comparison tomography of south-facing slope using different starting models (linear versus layered). All models produce low mean squared errors. Despite differences in color scale, all models show bedrock at 4-6 m depth.

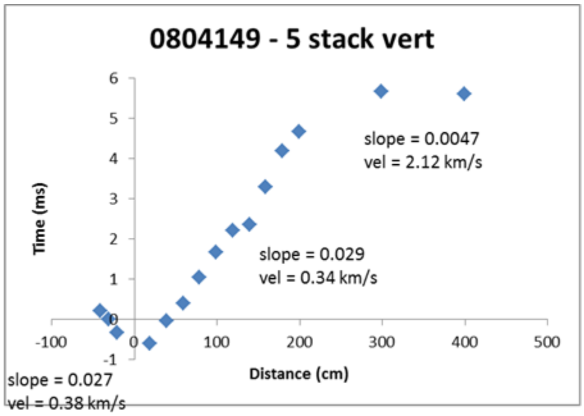

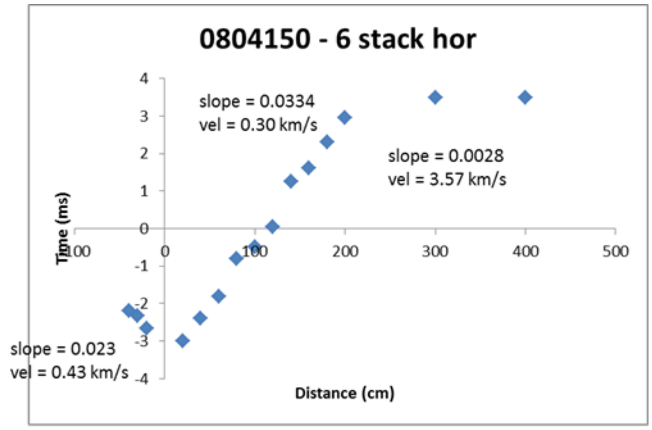

Figure S5. Distance versus time plots for surveys collected near the open pit at the base of the south facing slope of SSHO.

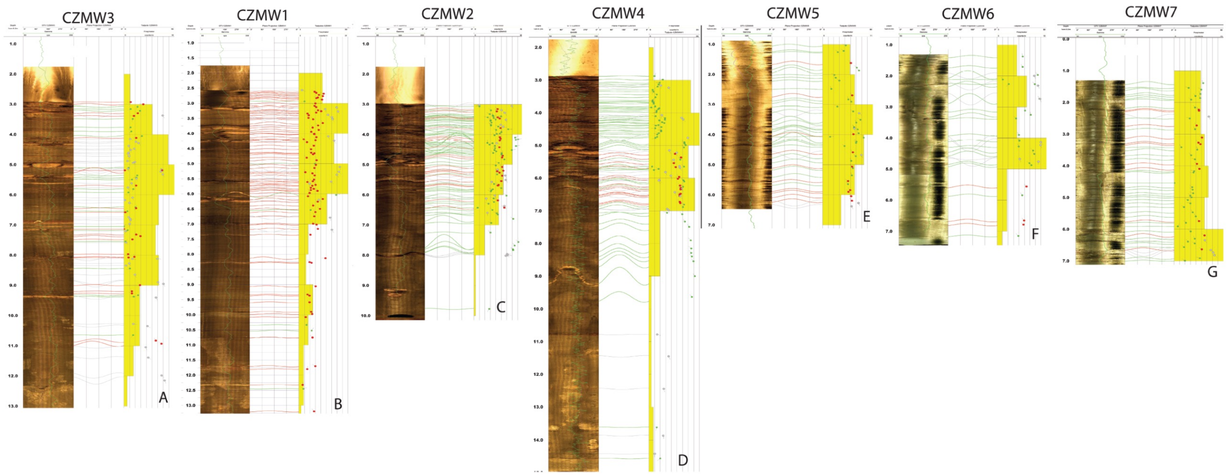

Figure S6. Optical televiewer logs of monitoring wells completed at SSHO. Fractures were picked from OTV logs using WellCad 4.3 (Advanced Logic Technology). Red and green lines show locations and dip magnitudes of major fractures. Tadpoles show fracture dip direction and fracture counts. Yellow bins show fracture densities (frequency/meter) with depth. A) OTV log of CZMW3, B) CZMW1, C) CZMW2, D) CZMW3, E) CZMW5, F) CZMW6, G) CZMW7. OTV logs for the Lynch well and CZMW8 are omitted because of lack of clear data in the upper meters of the wells. Amplitude of fractures reflect fracture dip angle.

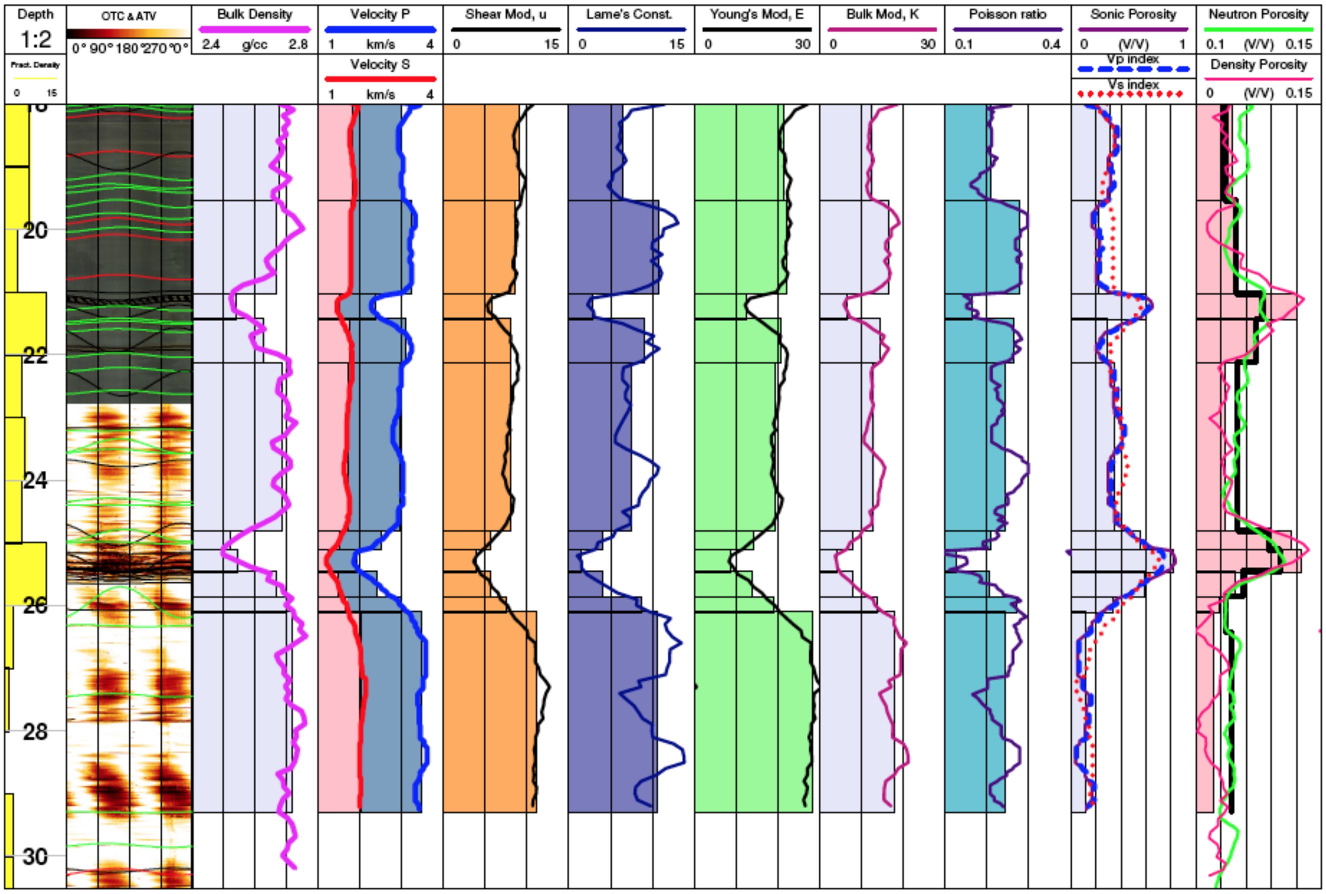

Figure S7. Borehole geophysical data for CZMW8, showing depth-correlated records of (left to right) observed bedrock/fracture distributions (OTV data) rock-mass density, seismic velocities and elastic properties, and multiple measures/scales of porosity. Lines are measured data, filled boxes are averaged data for each zone.